Synthetic Satellite Imagery for Real-Time High-Resolution Model Evaluation

DAN BIKOS,* DANIEL T. LINDSEY,[+] JASON OTKIN,[#] JUSTIN SIEGLAFF,[#]
LOUIE GRASSO,* CHRIS SIEWERT,[@] JAMES CORREIA JR.,[@] MICHAEL CONIGLIO,[&]
ROBERT RABIN,[#,&] JOHN S. KAIN,[&] AND SCOTT DEMBEK[@]

* Cooperative Institute for Research in the Atmosphere, Fort Collins, Colorado
[+] NOAA/NESDIS/STAR/RAMMB, Fort Collins, Colorado
[#] Cooperative Institute for Meteorological Satellite Studies, University of Wisconsin—Madison, Madison, Wisconsin
[@] Cooperative Institute for Mesoscale Meteorological Studies, University of Oklahoma, Norman, Oklahoma
[&] National Severe Storms Laboratory, Norman, Oklahoma

ABSTRACT

Output from a real-time high-resolution numerical model is used to generate synthetic infrared satellite imagery. It is shown that this imagery helps to characterize model-simulated large-scale precursors to the formation of deep-convective storms as well as the subsequent development of storm systems. A strategy for using this imagery in the forecasting of severe convective weather is presented. This strategy involves comparing model-simulated precursors to their observed counterparts to help anticipate model errors in the timing and location of storm formation, while using the simulated storm evolution as guidance.

1. Introduction

More than two decades ago, Schiavone and Papathomas (1990) stressed the need for efficient methods of visualizing output from numerical weather prediction (NWP) models. As the volume of this output continues to increase at a rapid rate, the need for efficiency is more pressing than ever. Plots of NWP output fields onto a map were first made possible for operational use in 1958 at the National Meteorological Center, now known as the National Centers for Environmental Prediction (NCEP) (Shuman 1989). Advances in computer imaging led to a transition in visualization from relatively crude gray-shaded line maps to color computer images (Hasler et al. 1985; Hibbard et al. 1994). As computing power continues to increase, it is now possible to generate more computationally expensive model-derived fields, such as infrared brightness temperatures and radar reflectivity, and to display these data in a manner consistent with typical satellite and radar visualization methods. This is advantageous because forecasters are already accustomed to diagnosing the state of the atmosphere by viewing animations of radar and satellite data. The key

to this visualization technique is animated imagery, as this is a particularly useful way of viewing large amounts of data (Grotjahn and Chervin 1984). Satellite data are most valuable when they are animated and enhanced with a color table (Suchman et al. 1981).

The synthetic satellite imagery discussed in this paper is similar to that described in Grasso et al. (2008) and Otkin et al. (2009). The imagery is generated by passing output from an NWP model through a forward radiative transfer model capable of computing realistic radiances for different spectral bands. Synthetic imagery has existed for some time (e.g., Chevallier et al. 2001, Chevallier and Kelly 2002, Raymond and Aune 2003; Otkin and Greenwald 2008) and has been used by operational forecasters [e.g., the Cooperative Institute for Meteorological Satellite Studies (CIMSS) Regional Assimilation System; Diak et al. (1995)] but not at convection-allowing scales. The utility of synthetic satellite imagery on these scales as a tool to forecast thunderstorms is examined in this study. Advantages gained from using synthetic satellite imagery include 1) an integrated view of the atmosphere that is provided more quickly than can be attained by looking at individual model output fields and then integrating them mentally to get a 3D perspective; 2) identification of features that are important to thunderstorm development, such as cloud cover and midlevel short waves, in a manner consistent with Geostationary Operational Environmental

Satellite (GOES) imagery, making their diagnosis more intuitive and efficient; and 3) the means for comparing model output with GOES imagery at high temporal intervals before convective initiation. These advantages directly relate to the goals of Schiavone and Papathomas (1990), that is, to fully exploit the ultimate value of meteorological data within the time constraints of operational forecasting.

There are numerous applications of synthetic satellite imagery to weather forecasting, such as winter weather, orographic cirrus, cyclogenesis, and general sky cover. This study focuses on its role in severe thunderstorm forecasting using a semioperational NWP model. The primary motivation for utilizing the synthetic imagery for severe thunderstorm forecasting is twofold: 1) for forecasters at the Storm Prediction Center (SPC) to quickly evaluate model output by viewing it as familiar satellite imagery loops and 2) to evaluate the product and familiarize forecasters with the new Advanced Baseline Imager (ABI) spectral bands during the SPC Spring Experiment at the Hazardous Weather Test Bed (HWT; Clark et al. 2012), as part of the GOES-R Proving Ground (Goodman et al. 2012, hereafter GBAMS; Reed et al. 2011). The ABI, to be launched on board the GOES-R geosynchronous satellite, will have improved spatial, temporal, and spectral resolutions compared to the current GOES data (Schmit et al. 2005), with the synthetic satellite imagery corresponding to the infrared bands on the ABI. This paper will address characteristics of the synthetic satellite imagery, including its production from high-resolution model output in real time, examples that highlight its strengths and weaknesses, and its operational utilization. Section 2 describes the methodology, examples are provided in section 3, and section 4 presents information on how the product evolved into a semioperational product (the GOES-R Proving Ground project) and associated training efforts.

2. Methodology

a. Numerical model data

In collaboration with the National Severe Storms Laboratory (NSSL), the Advanced Research core of the Weather Research and Forecasting Model (WRF-ARW; Skamarock et al. 2005) forecasts produced daily at NSSL (Kain et al. 2010) are being used to generate near-real-time synthetic satellite imagery every hour from 9 to 36 h into the forecast period. The first 8 h of output are omitted due to model spinup and the length of time required to run the model and generate the synthetic imagery. The NSSL-WRF has 4-km horizontal grid spacing and does not parameterize moist convection; that is,

convective clouds are explicitly simulated on the model grid. Cloud microphysical processes are parameterized using the WRF single-moment six-class microphysics scheme (WSM6; Hong and Lim 2006), which is a single-moment package that predicts the mass of cloud water, cloud ice, snow, graupel, and rain at every three-dimensional grid box. Additional details about the NSSL-WRF can be found in Kain et al. (2010).

b. Synthetic imagery generation

As part of the GOES-R Proving Ground, synthetic imagery is being generated at the Cooperative Institute for Research in the Atmosphere (CIRA) at Colorado State University and at the CIMSS at the University of Wisconsin—Madison. Select fields from the NSSL-WRF are used as inputs to a forward radiative transfer model (RTM) that is used to compute the top-of-the-atmosphere brightness temperatures for a given ABI infrared band. The term forward model refers to an RTM that takes into account surface, atmospheric, and cloud properties and predicts what radiance and brightness temperatures a satellite will observe. At CIRA, the brightness temperatures were computed using the delta-Eddington two-stream (Deeter and Evans 1998) RTM, whereas the successive order of interaction (Heidinger et al. 2006) RTM was employed at CIMSS. Details for each RTM can be found in the appendix. Although some differences exist between the simulated imagery produced at CIRA and CIMSS, these differences are typically much smaller than the differences between the synthetic imagery and real GOES observations. Since the primary goal of this paper is to describe how to qualitatively use synthetic satellite imagery to identify atmospheric features in model output, a detailed comparison of the imagery is beyond the scope of this paper. All meteorological features discussed in section 3 are equally evident in both forward-model solutions.

Brightness temperatures for each ABI infrared band (nine total, 6.185–13.3 μm) are calculated at CIMSS, and a subset of those (6.185, 6.95, 8.5, 10.35, and 12.3 μm), in addition to the 3.9-μm band, are generated at CIRA. For the 3.9-μm band, the solar-reflected component is too computationally expensive to be produced in real time, so only the emitted component is generated. When solar radiation is involved, multiple scattering among cloud particles must be taken into account, and the result is at least an order of magnitude increase in the total number of calculations. Once the brightness temperatures are calculated for a given band, the forecast imagery is converted to Man-computer Interactive Data Access System (McIdas) format (Lazzara et al. 1999) for use in the SPC's and Hydrometeorological Prediction Center's (HPC) NCEP Advanced Weather Interactive Processing System

(N-AWIPS), and to network common data form (netCDF) format for the National Weather Service (NWS) AWIPS system. Output is made available to the SPC, HPC, and a number of NWS offices (those currently participating in the GOES-R Proving Ground) to assist in their daily forecasts. In addition to the synthetic ABI bands, a few band differences are also being produced for evaluation. For example, the split-window difference (10.35–12.3 μm) is used to highlight areas of low-level water vapor convergence (Chesters et al. 1983), providing potentially useful information on convective initiation locations before any clouds have formed. An example of this difference is provided in section 3.

3. Examples

Five examples are shown to highlight representative strengths and weaknesses of using synthetic imagery from the NSSL 4-km WRF-ARW for severe thunderstorm forecasting. The example in section 3d utilizes the CIMSS forward model, while the examples in the other sections utilize the CIRA forward model.

a. 21 June 2010: Jet streak–short-wave identification

The first example highlights one of the primary uses of the synthetic water vapor imagery—the identification of jet streaks and short-wave troughs that may play a role in the initiation, maintenance, and intensity of deep convection. As jet streaks become juxtaposed with low-level convergence boundaries, they can play a role in convective initiation (Beebe and Bates 1955). Analysis of jet streaks in animated synthetic water vapor imagery utilizing methods such as those described in Weldon and Holmes (1991) can be combined with model output fields (i.e., isotachs at a given pressure level) to efficiently identify the jet streak of interest. Short waves can be identified in water vapor imagery by cyclonic flow accompanied by a sharp brightness temperature gradient. This gradient is due to rising motion ahead of the trough axis leading to cooling and moistening, while sinking motion behind the trough results in warming and drying.

Figure 1 shows the synthetic water vapor imagery computed using the CIRA forward-modeling system along with corresponding *GOES-13* water vapor imagery at 1700 UTC 21 June and 0100 UTC 22 June 2010. The synthetic brightness temperatures are warmer than the observed *GOES-13* brightness temperatures for clear-sky regions. One reason for this is a disparity in wavelength between synthetic and actual observations. Specifically, the synthetic imagery is derived on the basis of the GOES-R ABI 6.95-μm band while the *GOES-13* water vapor band has a central wavelength of 6.5 μm. The weighting function for the 6.95-μm band peaks lower in

the atmosphere than the 6.5-μm band, inherently favoring warmer clear-sky brightness temperatures in the synthetic imagery. However, despite these systematic differences, it is still straightforward to compare the synthetic and observed water vapor bands to locate mid- and upper-level features of interest.

At 1700 UTC there is an upper-level low over western Montana and a short-wave trough that appears as a region of warmer brightness temperatures in Nebraska and South Dakota (annotated in Fig. 1a) west of a line of clouds in Minnesota and Iowa. The authors recommend that readers view the animated synthetic imagery (along with WRF-ARW upper-level fields) and animated *GOES-13* imagery using the URL provided in the caption for Fig. 1 to more easily identify these features. The animated imagery also depicts a region of relatively fast-moving cooler brightness temperatures from Arizona into Colorado associated with a jet streak. By 0100 UTC, eastward expansion of warmer brightness temperatures in the northern plains reveals the northeastward migration of the short-wave trough, and a significant expansion of the cooler brightness temperatures along the leading edge reflects the development of a mesoscale convective system (MCS; Houze 2004; see Figs. 1b,d) in Wisconsin and Illinois. Cooler cloud tops did not expand as rapidly or grow as large in the synthetic imagery compared to the *GOES-13* observations, even though an area of widespread storms did develop along the leading edge of the short-wave trough in the model. The sizes of convectively generated cold-cloud shields and anvil outflow areas generated by the NSSL-WRF (and other similarly configured WRF models) tend to be too small compared to the observations, which is likely related to deficiencies in currently available microphysical parameterizations (e.g., see Weisman et al. 2008).

Three simulated corridors of dry air (Fig. 1a), one extending from Colorado into eastern Nebraska, one extending from New Mexico into western Oklahoma, and another stretching from Louisiana to Alabama, correspond to similar locations in the observed imagery (Fig. 1c). Likewise, the corridors of higher moisture extending from Minnesota southward into Iowa and through Indiana and Ohio are well placed as the model attempts to maintain and develop convection in those regions. However, the model is too fast in clearing away the cloud field in southwestern Minnesota. Regarding the jet streak spreading over the Rockies into the central plains, the model develops convection along its leading edge, similar to what was observed. Monitoring processes relative to features that are well resolved and properly depicted in the synthetic imagery can have value in an operational forecasting environment.
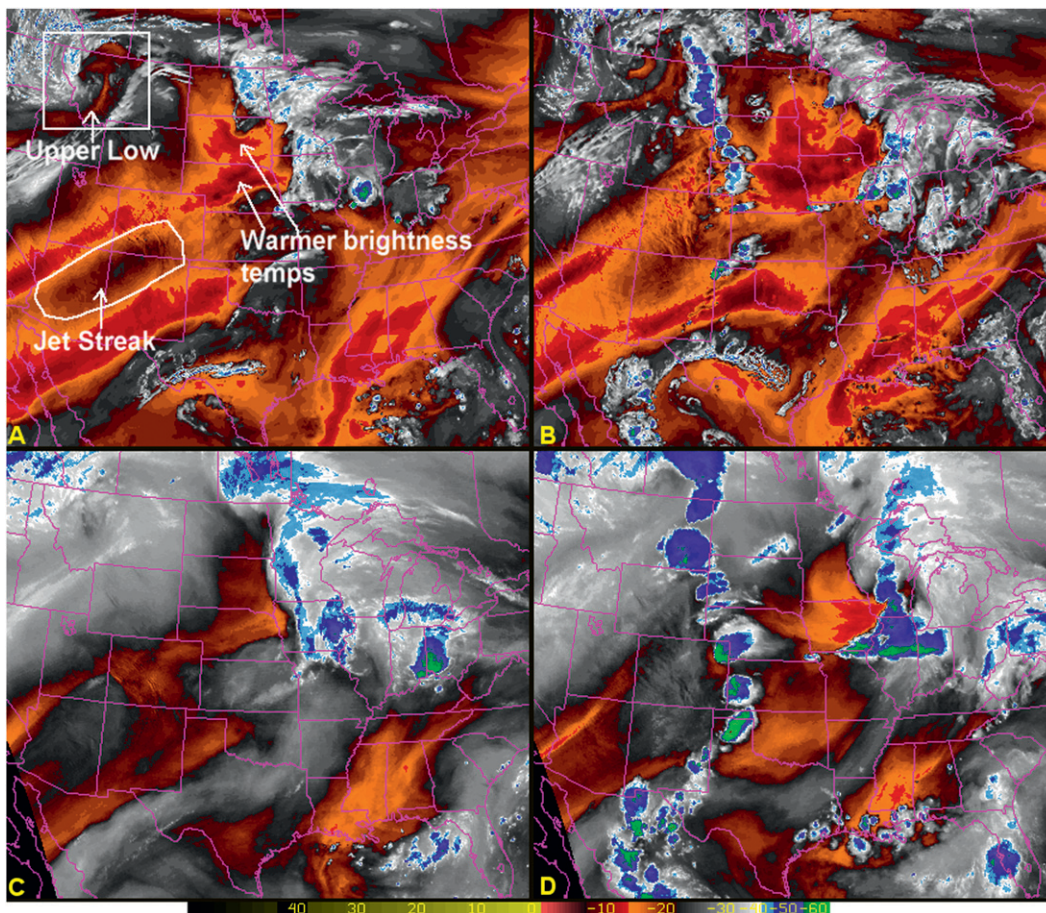
FIG. 1. NSSL 4-km WRF-ARW synthetic satellite imagery for the 6.95-μm (water vapor) band from the 0000 UTC 21 Jun 2010 model run valid at (a) 1700 and (b) 0100 UTC 22 Jun. *GOES-13* imagery for the 6.5-μm (water vapor) band at (c) 1703 and (d) 0102 UTC 22 Jun. The brightness temperature scale (°C) is the same for the synthetic and GOES imagery. Animated loops between 1200 and 0100 UTC are also available for the synthetic imagery along with overlays for 250- and 500-hPa geopotential heights (m), along with 250-hPa isotachs (m s^{-1}) (http://rammb.cira.colostate.edu/ redirect/21jun10_synth_band9) and the GOES imagery (http://rammb.cira.colostate.edu/redirect/21jun10_goes_wv).

b. 20 June 2010: Cloud cover forecast

This case demonstrates how synthetic IR imagery can be used to evaluate the impact of cloud cover when forecasting a severe weather event. The synthetic imagery in Fig. 2a depicts a large area of low-level clouds (as slightly colder brightness temperatures) across Nebraska, northeast Colorado, and portions of eastern Wyoming during the morning of 20 June 2010. By 1900 UTC (Fig. 2b), the low-level clouds are forecast to dissipate in western Nebraska and Wyoming. Across northeast Colorado into Nebraska, high clouds are forecast, which makes the low-level clouds more difficult to see, but the animated imagery shows the clouds in this region dissipating by 2200 UTC. By 2300 UTC (Fig. 2c), thunderstorm development is forecast across eastern Wyoming, western Nebraska, and northeast Colorado. The easiest way to

see the cloud evolution is by viewing the higher temporal resolution animated imagery; links to the animations are provided in the Fig. 2 caption. The corresponding *GOES-13* imagery in Figs. 2d–f depicts low-level clouds dissipating across portions of Wyoming, with thunderstorm development in southeast Wyoming by 1902 UTC. However, the *GOES-13* imagery also shows low-level clouds persisting in the western Nebraska panhandle and northeast Colorado where the NSSL-WRF had forecast low cloud dissipation. This cloud field significantly reduced insolation across these areas, resulting in surface temperatures 5°–10°C colder than forecast by the WRF-ARW (Fig. 3). By 2302 UTC thunderstorms were ongoing in Wyoming and northwest Kansas, but none occurred in northeast Colorado and western Nebraska, where the NSSL-WRF had forecast thunderstorm development. This example demonstrates how
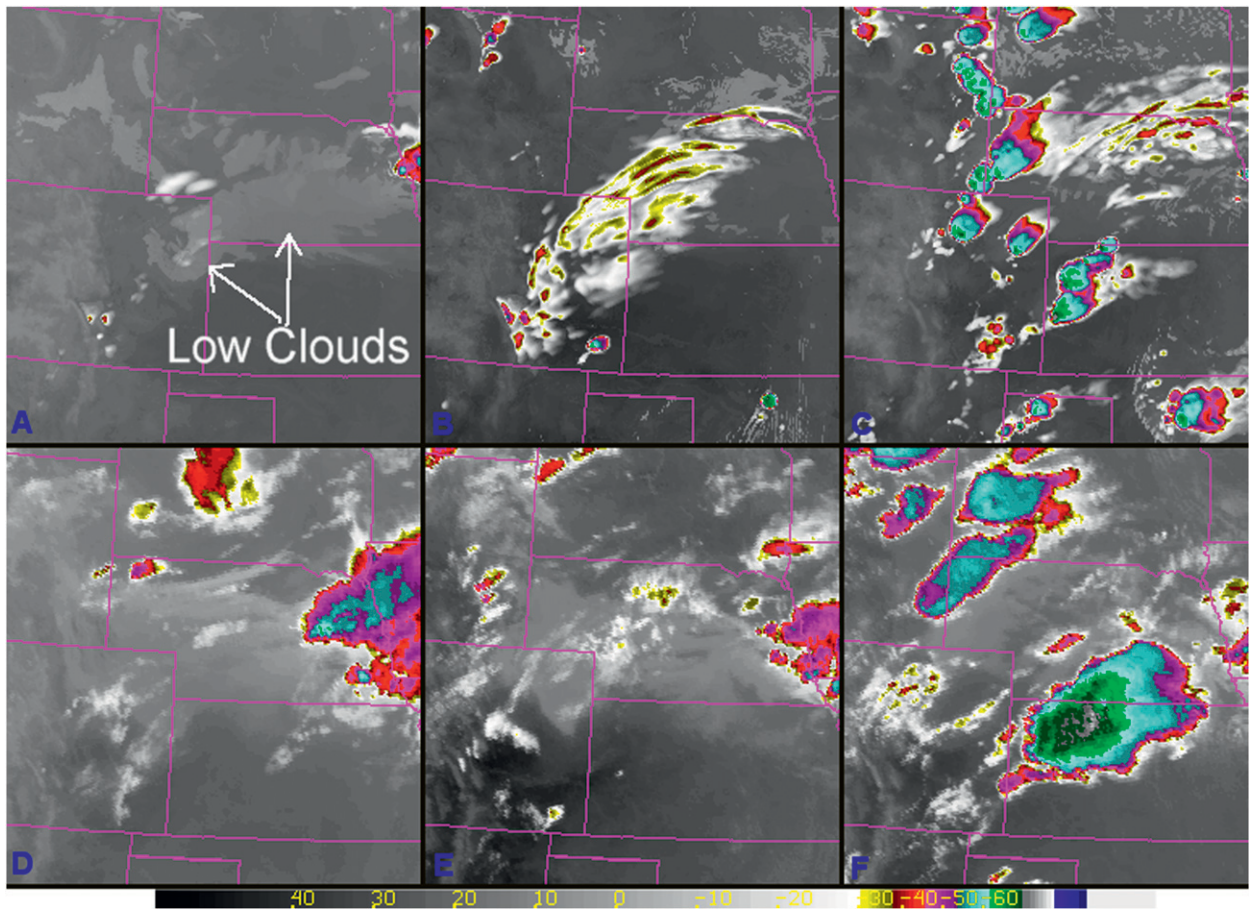
FIG. 2. NSSL 4-km WRF-ARW synthetic imagery for the 10.35-μm (IR) band from the 0000 UTC 20 Jun 2010 model run valid at (a) 1400 and (b) 1900 UTC, and (c) 2300 UTC. *GOES-13* imagery for the 10.7-μm (IR) band at (d) 1402, (e) 1902, and (f) 2302 UTC. The brightness temperature scale (°C) is the same for the synthetic and GOES imagery. Animated loops between 1200 and 0000 UTC are also available for the synthetic imagery (http://rammb.cira.colostate.edu/redirect/20jun10_synth_band13) and the GOES imagery (http://rammb.cira.colostate.edu/redirect/20jun10_goes_ir).

synthetic satellite imagery can be used to evaluate model performance during the morning hours and then monitor trends in the GOES IR (or visible) imagery during the day to assess how much confidence one should have in the model forecasted thunderstorm evolution.

c. 12 May 2010: Cirrus cloud considerations and MCS appearance

As discussed in section 2 above, the WSM6 single-moment microphysics package requires that assumptions be made about cloud particle number concentrations, which can lead to errors in the cloud optical depths computed by the forward radiative transfer model and introduce errors in the synthetic satellite imagery. The impact of these errors is that relatively thin cirrus clouds depicted in the synthetic imagery are sometimes warmer or colder than observed. The optically thinner (thicker)

clouds allow more (less) radiation from below to pass through and this increases (decreases) the top-of-the-atmosphere brightness temperatures. In addition to the optical depth issue, the NSSL-WRF sometimes generates unnatural-looking linear streaks of cirrus clouds. Figure 4a shows an example of a long, cold streak of cirrus clouds in the synthetic imagery (extending across the panhandles of Texas and Oklahoma into southern Kansas). Typically, the forecast location of the cirrus clouds will be reliable, but the optical depth and linear, thin nature of the clouds are less reliable.

Figure 5 shows another example of MCS appearance in the synthetic imagery. As with other cases, the cirrus canopy forecast by the NSSL-WRF model is not continuous and the areal extent of the cold cloud tops is vastly underdone. Nonetheless, the associated reflectivity pattern and rain locations may still be accurate in the model forecast.
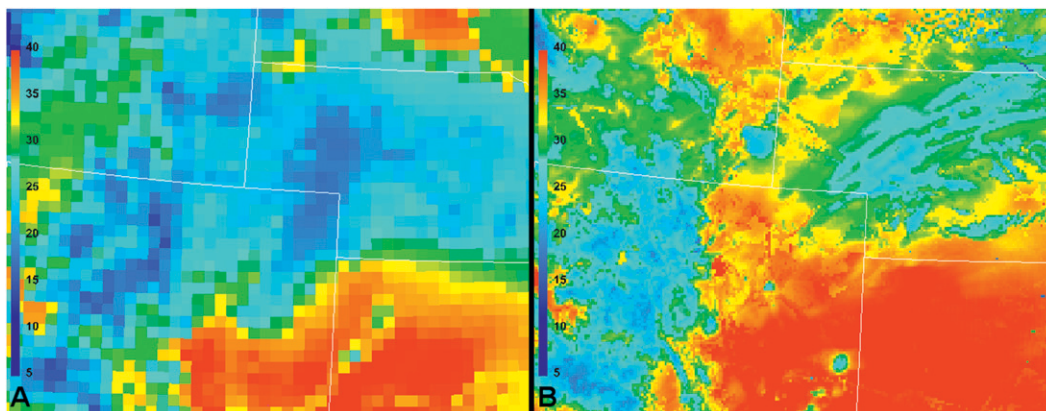
FIG. 3. Surface temperature (°C) at 2100 UTC 20 Jun 2010 from the (a) Rapid Update Cycle (RUC) 0-h analysis and (b) NSSL WRF-ARW 21-h forecast.

d. 8 June 2011: Convective initiation

This case highlights how synthetic satellite imagery can influence forecaster confidence in a model solution of convective initiation when ongoing convection complicates longer-range forecasts. For this case, a strong cold front and associated thunderstorms were forecast by the NSSL-WRF to move across the upper Mississippi River valley during the evening of 8 June 2011. Although the large-scale conditions were conducive to thunderstorm development, forecasters participating in the HWT Spring Experiment (described in section 4) were initially concerned that cloud cover associated with morning convection across southern Wisconsin and northern Illinois (Fig. 6d) would hinder the growth of stronger daytime

instability and, therefore, decrease the potential for thunderstorm development later in the day. Inspection of the synthetic satellite imagery showed that the NSSL-WRF model depicted the overall coverage and intensity of the morning thunderstorm activity reasonably well (Fig. 6a), which increased forecaster confidence that thunderstorms would redevelop later in the forecast period despite the extensive morning cloud cover.

The synthetic satellite imagery indicated that the cloud cover would dissipate by early afternoon and that convective initiation would occur along the cold front over southwest Wisconsin by 2100 UTC (Fig. 6b) with upscale development into an intense squall line by 0200 UTC 9 June (Fig. 6c). Higher forecast confidence in this scenario was justified based on the corresponding *GOES-13*
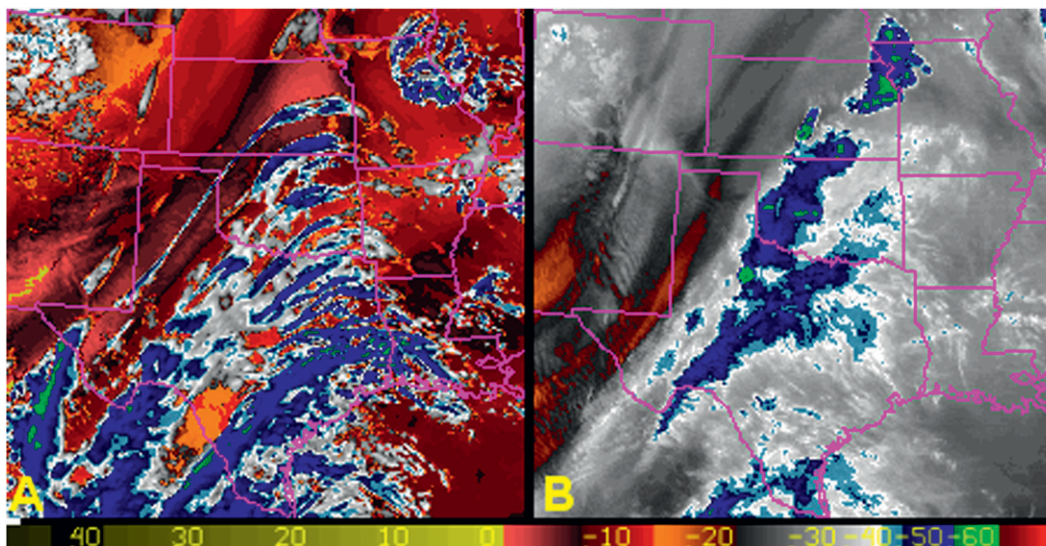

FIG. 4. (a) NSSL 4-km WRF-ARW synthetic imagery for the 6.95-μm (water vapor) band from the 0000 UTC 12 May 2010 model run valid at 2000 UTC. (b) *GOES-13* 6.5-μm (water vapor) band at 2002 UTC 12 May 2010. The brightness temperature scale (°C) is the same for the synthetic and GOES imagery.
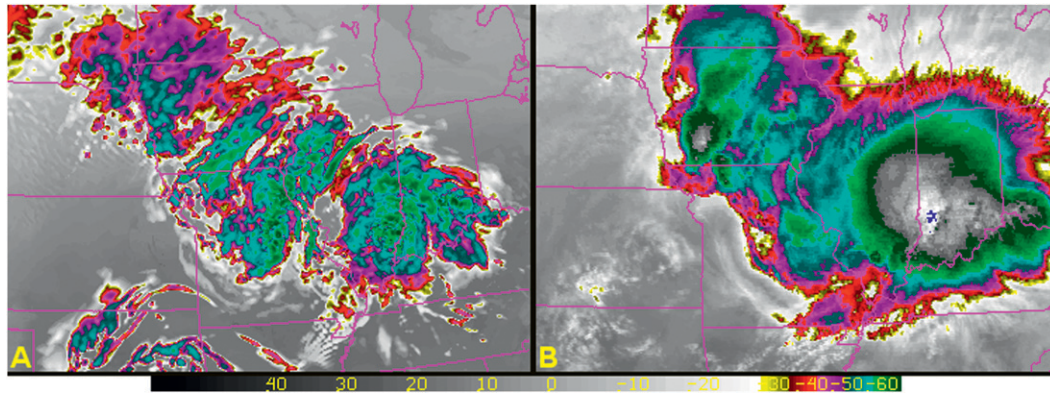
FIG. 5. (a) NSSL 4-km WRF-ARW synthetic imagery for the 10.35-μm (IR) band from the 0000 UTC 12 May 2010 model run valid at 1200 UTC. (b) *GOES-13* 10.7-μm (IR) band at 1232 UTC 12 May 2010. The brightness temperature scale (°C) is the same for the synthetic and GOES imagery.

observations showing initial thunderstorm development across southwest Wisconsin by 2130 UTC (Fig. 6e). During the next several hours, a strong squall line developed from eastern Iowa northeastward across southern Wisconsin (Fig. 6f). Many severe wind reports occurred across this region. Although the thunderstorms developed too far to the southwest in the NSSL-WRF forecast, the synthetic satellite imagery generally agrees well with the *GOES-13* observations over eastern Iowa, southeastern Wisconsin, and northern Illinois.

Overall, forecasters using the synthetic satellite imagery had greater confidence that thunderstorms would develop later in the day because the model correctly captured the morning convection and showed that sufficient atmospheric recovery would occur during the afternoon. Extensive morning cloud cover often complicates forecasts for afternoon or evening convection and typically reduces the potential for severe thunderstorms because the decrease in insolation limits the growth of surface-based instability that contributes to thunderstorm development. If the NSSL-WRF forecast had shown sunny skies across Wisconsin during the morning rather than the extensive cloud cover that actually occurred, then the forecasters may have had less confidence that convection would develop during the evening since they would have to consider the possibility that the model overestimated the magnitude of the potential instability that developed later in the day.

e. 20 April 2011: Band differencing

Prior work (e.g., Chesters et al. 1983) has shown that band differences may be valuable in determining the timing and location of convection initiation. Figure 7 shows an example of the 10.35–12.3-μm difference product. Water vapor preferentially absorbs radiation at 12.3 μm relative to 10.35 μm, and assuming the low-level temperatures

decrease with height, areas of deeper water vapor will have more positive 10.35–12.3-μm brightness temperature differences (Chesters et al. 1983). The magnitude of the difference depends on the water vapor distribution, the temperature profile, and the surface emissivity, but the water vapor effect can be isolated by viewing the change of the brightness temperature difference with time. Deepening water vapor associated with low-level convergence will then appear as local maxima increasing with time. In this example, an east–west-oriented line of positive values (yellow to orange to red indicates increasing positive values) is evident across central Texas in a cloud-free region. By 1800 UTC, convective clouds have begun to form, and convective initiation occurs there around 1900 UTC. This product may be used as a tool to quickly determine where the model places low-level water vapor convergence. Additionally, it serves as a proof of concept that this field could be quite useful in forecasting cloud and convection formation locations. Water vapor retrievals will be performed as part of the standard GOES-R suite of products, but it remains to be seen whether small-scale moisture gradients will be as evident in these retrievals as with the simple band difference technique.

4. Utilization of simulated imagery as a semioperational product

The GOES-R Proving Ground (http://cimss.ssec.wisc. edu/goes_r/proving-ground.html) within NOAA National Centers, such as the SPC, as well as various NWS Weather Forecast Offices (WFOs), attempts to prepare the user community for the launch of GOES-R (GBAMS; Reed et al. 2011). To prepare users for products and capabilities that will be available on GOES-R, demonstrations and training in semioperational settings need to be
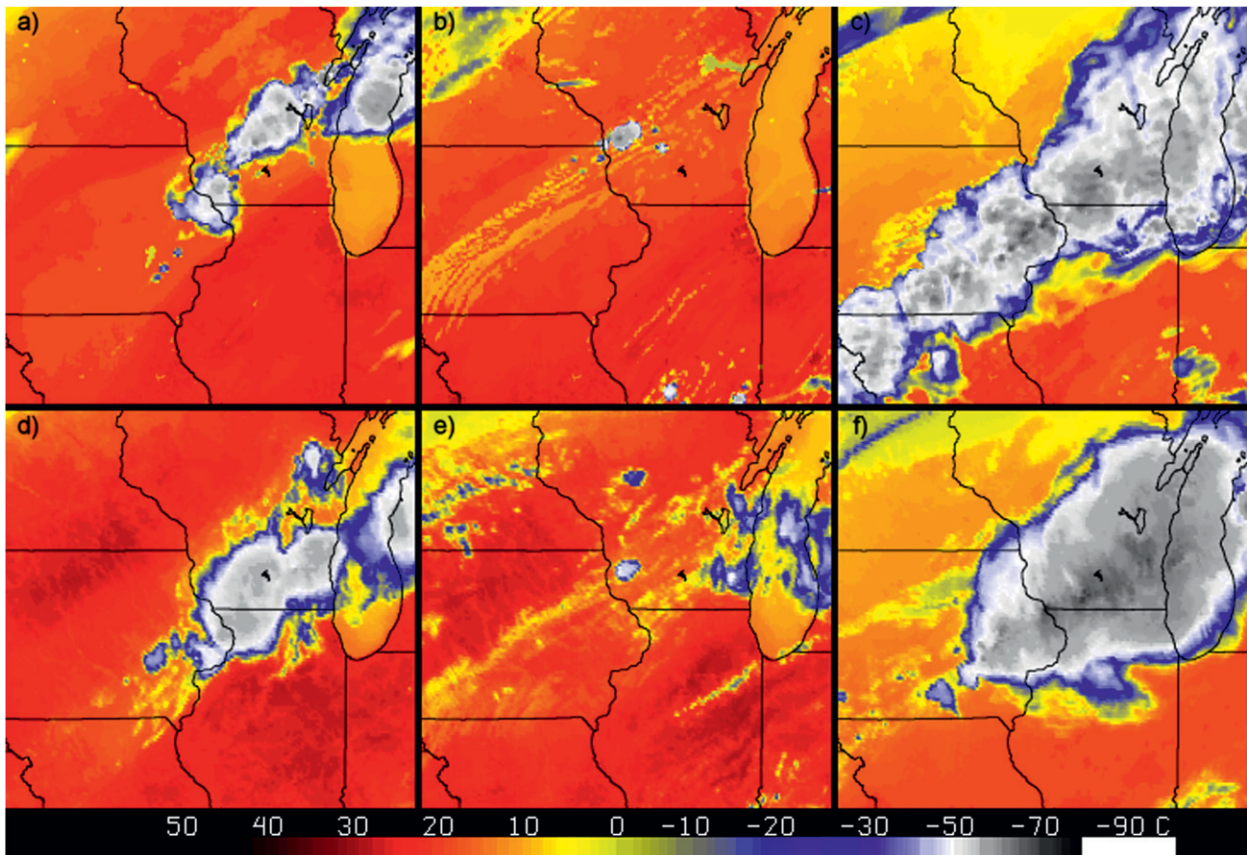
FIG. 6. NSSL 4-km WRF-ARW synthetic imagery for the 11.2-μm (IR) band from the 0000 UTC 8 Jun 2011 model run valid at (a) 1500 UTC 8 Jun, (b) 2100 UTC 8 Jun, and (c) 0200 UTC 9 Jun 2011. *GOES-13* imagery for the 10.7-μm (IR) band at (d) 1515 UTC 8 Jun, (e) 2132 UTC 8 Jun, and (f) 0202 UTC 9 Jun 2011. The brightness temperature scale (°C) is the same for the synthetic and *GOES-13* imagery. Animated loops between 1400 UTC 8 Jun and 0300 UTC 9 Jun 2011 are also available for the synthetic imagery (http://cimss.ssec.wisc.edu/goes_r/proving-ground/nssl_abi/08june2011/08june2011_abi_ir.html) and the GOES imagery (http://cimss.ssec.wisc.edu/goes_r/proving-ground/nssl_abi/08june2011/08june2011_goes_ir.html).

accomplished. Forecasters at the SPC are exposed to experimental GOES-R Proving Ground products, such as the synthetic satellite imagery, within their operational N-AWIPS systems. In addition, a yearly spring experiment takes place within the HWT (Clark et al. 2012), where new products and techniques that assist in the forecasting of severe weather are demonstrated for a period of several weeks.

Participants at the 2011 Spring Experiment were exposed to the entire suite of synthetic imagery, which included all nine infrared ABI bands, as well as multiple unique GOES-R band differences described in section 2b. Forecasters were provided with the synthetic imagery by approximately 1400 UTC daily, which was prior to their morning forecasting operations, with the band differences arriving about an hour later.

Synthetic water vapor imagery was used during the forecast exercises to identify the position of upper lows and short-wave troughs and their accompanying moist and dry areas, and to assess the timing of such features and the placement of existing convection relative to concurrent observations. This general approach was applied daily during a 5-week period. Subjective verification indicated that when the features matched well in space at a given time, the forecasters had increased confidence in the model solution for subsequent forecast periods. Once the comparison was made, and the features were deemed acceptable for subjective analysis, the synthetic imagery was animated. The timing of features of interest, such as first indications of convective cloud tops, or the anticipation of trends in drying or moistening due to synoptic-scale processes were noted.

The synthetic imagery served as a starting point in the analysis of the convection-allowing model output and offered a unique perspective on the main features of the day, if they were synoptic in origin. Of course, the converse is true as well; if the imagery indicated very little discernible large-scale impact on the region of interest,
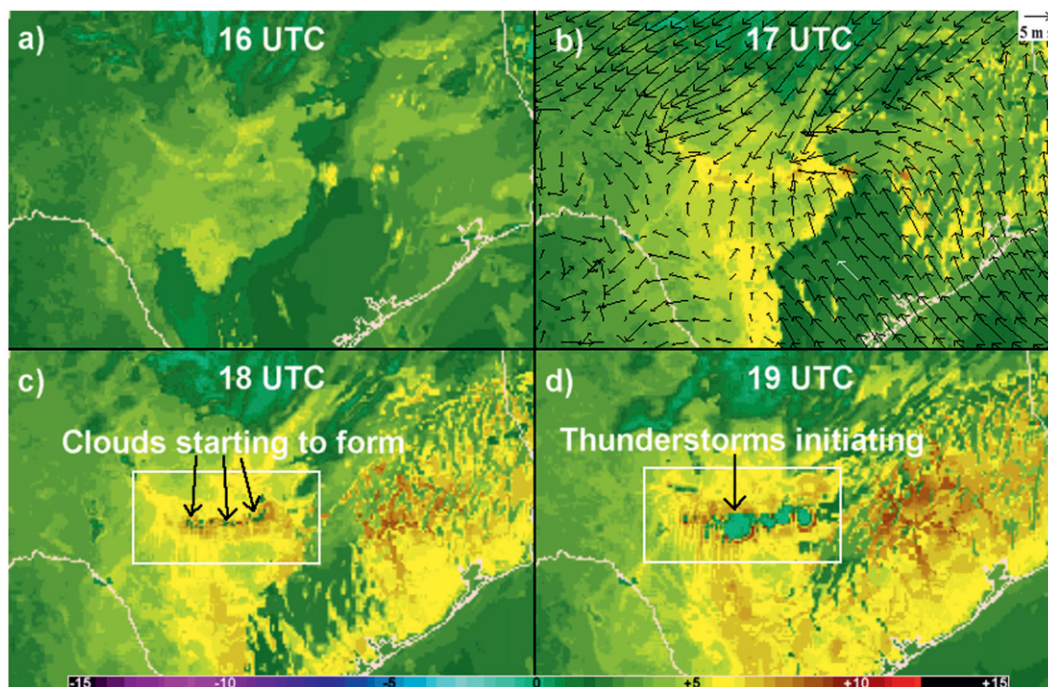
FIG. 7. Synthetic 10.35–12.3-μm band from the NSSL WRF 0000 UTC 20 Apr 2011 (a) 16-, (b) 17-, (c) 18-, and (d) 19-h forecasts. The brightness temperature difference scale in °C. Warmer colors represent more positive values. The images appear as they do in N-AWIPS, the operational display software at the SPC. The vectors in (b) are the 10-m winds from the NSSL WRF and the green areas within the boxes in (c) and (d) are convective clouds.

then this alerted the forecasters to the importance of mesoscale details on the subsequent convective evolution. The length of time for analysis of this specific forecast field was typically less than 10 min (including comparison and animation of the forecast). On many occasions the imagery proved valuable and thus quickly became part of the forecast routine. Later in the forecast process, forecasters often requested the imagery even after additional model fields were examined. In these cases, the small-scale details that were identified using other model fields needed to be considered within the context of the larger scales that the imagery provided.

The simulated band differencing was not utilized as frequently as the other synthetic fields, but proved capable of identifying bands of deepening moisture up to several hours prior to convection initiation. Although validation is still under way, when used as a supplement to other model fields that can identify convergence bands in the boundary layer, the band difference product showed promise in discriminating the convergence bands along which convection was possible from the more benign boundary layer convergence bands in the model. If this impression proves accurate, then this field could be quite useful in identifying potentially active boundaries in the real atmosphere once it is available in the suite of GOES-R observational products.

An important step in the transition to a semioperational product is the training of the on the application of the product. The Virtual Institute for Satellite Integration Training (Mostek et al. 2004) has developed a training module for the use of the synthetic imagery in severe weather forecasting. The training module informs users about some of the strengths and weaknesses, such as those discussed in section 3, along with basic knowledge of how the product is produced and operational concerns such as when the product is available to view. The training was delivered in February 2011 to the SPC via live teletraining to 27 staff members before the start of the severe weather season. A recorded version is also available online (http://rammb.cira.colostate.edu/training/visit/training_sessions/synthetic_imagery_in_forecasting_severe_weather/) so that forecasters at WFOs participating in the GOES-R Proving Ground may participate in the training at their convenience.

5. Summary

As part of the GOES-R Proving Ground, synthetic GOES-R ABI imagery is being generated in near–real time from daily runs of the NSSL WRF-ARW model and provided to the SPC, HPC, and GOES-R Proving Ground participating WFOs for evaluation. A primary goal of the

GOES-R Proving Ground is to prepare forecasters for new GOES-R ABI data *before* they become available, ensuring data are fully utilized by operations the first day the new satellite is turned on. The evaluation of synthetic satellite imagery in operational forecasting centers provides a new and unique means of evaluating high-resolution model output. The synthetic imagery allows forecasters to visualize atmospheric processes from an integrated perspective instead of the typical analysis of individual model output fields followed by mental integration.

Forecasters can employ their working knowledge of GOES imagery interpretation to very quickly use the synthetic imagery output to assess the accuracy (both timing and spatial extent) of model forecasted features. For example, short waves and jet streaks can easily be located in the synthetic water vapor imagery and compared to observed GOES imagery. Similarly, cloud coverage can be viewed in the synthetic imagery and compared to observed GOES imagery throughout the day, leading to increased or decreased forecaster confidence in the model solution based on GOES observations.

It is essential to properly train users (e.g., forecasters) before making such a product available. Training can identify some of the limitations of synthetic satellite imagery and show forecasters how to integrate it with other model output such as simulated radar reflectivity and surface precipitation fields. As high-resolution forecast and radiative transfer models are streamlined and computers continue to improve, synthetic satellite imagery should become a standard output field to assist users in model evaluation.

APPENDIX

Forward Radiative Transfer Model Descriptions

a. Synthetic imagery generation at CIRA

Similar to the methodology outlined in Grasso et al. (2008), WRF-ARW output from NSSL is used to generate synthetic GOES-R ABI imagery. As soon as the 9-h forecast is complete, the microphysical variables (cloud water, cloud ice, snow, graupel, and rain), in addition to the hourly fields of pressure, temperature, water vapor, heights, and canopy temperature, are sent to CIRA. First, pressure, temperature, and water vapor values are used by the optical path transmittance (OPTRAN; McMillin

et al. 1995) algorithm to calculate gaseous transmittance. Three absorbing gases are used in this calculation: simulated water vapor, climatological ozone, and carbon dioxide. Next, the single-scattering albedo and total extinction are calculated for all five hydrometeors using modified anomalous diffraction theory (Mitchell 2000). Since WSM6 is a single-moment scheme, only the mass mixing ratio of each hydrometeor is predicted. As a result, number concentrations for any given hydrometeor must be assigned. Particle size is proportional to the ratio of the mass to the number concentration; consequently, the number concentration assignment leads to some uncertainty in the particle sizes for all five hydrometeor types. However, for the infrared bands currently being generated by CIRA, brightness temperatures are relatively insensitive to particle size, except possibly thin cirrus (discussed in section 3c). Optical properties for all five hydrometeors are then combined with a number concentration weighting. This process yields one set of optical properties that is then combined with the gaseous optical depth. These values are then passed to the delta-Eddington two-stream radiative transfer model (Deeter and Evans 1998), which calculates the radiances at the desired ABI bands. To produce realistic imagery, monthly mean surface emissivity values for every band are included from a global dataset (Seemann et al. 2008).

b. Synthetic imagery generation at CIMSS

The 12–36-h NSSL-WRF forecast output is used to generate synthetic GOES-R ABI imagery at CIMSS. The radiance calculation for each ABI infrared band (nine total, 6.185–13.3 μm) involves several steps within the CIMSS forward-modeling system. First, CompactOPTRAN, which is part of the National Oceanic and Atmospheric Administration's Community Radiative Transfer Model (CRTM; Han et al. 2006), is used to compute gas optical depths for each model layer using simulated temperature and water vapor mixing ratio profiles and climatological ozone data. Effective particle diameters were calculated for a given cloud species (i.e., ice, snow, graupel, cloud water, or rainwater) using its mixing ratio and particle size distribution assumptions specific to the WSM6 scheme. Ice cloud absorption and scattering properties, such as extinction efficiency, single-scatter albedo, and full-scattering phase function, based on Baum et al. (2005), are subsequently applied to each frozen hydrometeor species (i.e., ice, snow, and graupel). A lookup table based on Lorenz–Mie calculations is used to assign the properties for the cloud water and rainwater species. Visible cloud optical depths are calculated separately for the liquid and frozen hydrometeor species, following the work of Han et al. (1995) and Heymsfield et al. (2003), respectively, and are subsequently

converted into infrared cloud optical depths by scaling the visible optical depths by the ratio of the corresponding extinction efficiencies. The surface emissivity over land is obtained from the Seemann et al. (2008) global emissivity database, whereas the water surface emissivity is computed using the CRTM Infrared Sea Surface Emissivity Model. Finally, the simulated skin temperature and atmospheric temperature profiles along with the layer gas optical depths and cloud-scattering properties, are input into the Successive Order of Interaction (SOI) forward radiative transfer model (Heidinger et al. 2006), which is used to compute the simulated brightness temperatures. Previous studies have shown that the forward model produces realistic infrared brightness temperatures for both clear- and cloudy-sky conditions (Otkin and Greenwald 2008; Otkin et al. 2009; Feltz et al. 2009).

REFERENCES

Baum, B. A., P. Yang, A. J. Heymsfield, S. Platnick, M. D. King, Y.-X. Hu, and S. T. Bedka, 2005: Bulk scattering properties for the remote sensing of ice clouds. Part II: Narrowband models. *J. Appl. Meteor.,* **44,** 1896–1911.

Beebe, R. G., and F. C. Bates, 1955: A mechanism for assisting the release of convective instability. *Mon. Wea. Rev.,* **83,** 1–10.

Chesters, D., L. W. Uccellini, and W. D. Robinson, 1983: Low-level water vapor fields from the VISSR Atmospheric Sounder (VAS) "split window" channels. *J. Climate Appl. Meteor.,* **22,** 725–743.

Chevallier, F., and G. Kelly, 2002: Model clouds as seen from space: Comparison with geostationary imagery in the 11-μm window channel. *Mon. Wea. Rev.,* **130,** 712–722.

——, P. Bauer, G. Kelly, C. Jakob, and T. McNally, 2001: Model clouds over oceans as seen from space: Comparison with HIRS/2 and MSU radiances. *J. Climate,* **14,** 4216–4229.

Clark, A. J., and Coauthors, 2012: An overview of the 2010 Hazardous Weather Testbed Experimental Forecast Program Spring Experiment. *Bull. Amer. Meteor. Soc.,* **93,** 55–74.

Deeter, M., and K. F. Evans, 1998: A hybrid Eddington singlescatter radiative transfer model for computing radiances from thermally emitting atmospheres. *J. Quant. Spectrosc. Radiat. Transfer,* **60,** 635–648.

Diak, G. R., R. A. Aune, D. A. Santek, and R. C. Dengel, 1995: Synthetic GOES infrared images based on the CIMSS Regional Assimilation System. Preprints, *11th Int. Conf. on Interactive Information Processing Systems for Meteorology, Oceanography, and Hydrology,* Dallas, TX, Amer. Meteor. Soc., 155–156.

Feltz, W. F., K. M. Bedka, J. A. Otkin, T. Greenwald, and S. A. Ackerman, 2009: Understanding satellite-observed mountain wave signatures using high-resolution numerical model data. *Wea. Forecasting,* **24,** 76–86.

Goodman, S. J., and Coauthors, 2012: The GOES-R Proving Ground: Accelerating user readiness for the next generation geostationary environmental satellite system. *Bull. Amer. Meteor. Soc.,* in press.

Grasso, L. D., M. Sengupta, J. F. Dostalek, R. Brummer, and M. DeMaria, 2008: Synthetic satellite imagery for current and future environmental satellites. *Int. J. Remote Sens.,* **29,** 4373–4384.

Grotjahn, R., and R. M. Chervin, 1984: Animated graphics in meteorological research and presentations. *Bull. Amer. Meteor. Soc.,* **65,** 1201–1208.

Han, Q., W. Rossow, R. Welch, A. White, and J. Chou, 1995: Validation of satellite retrievals of cloud microphysics and liquid water path using observations from FIRE. *J. Atmos. Sci.,* **52,** 4183–4195.

Han, Y., P. van Delst, Q. Liu, F. Weng, B. Yan, R. Treadon, and J. Derber, 2006: JCSDA Community Radiative Transfer Model (CRTM)-Version 1. NOAA Tech. Rep. NESDIS 122, 33 pp.

Hasler, A. F., H. Pierce, K. R. Morris, and J. Dodge, 1985: Meteorological data fields "in perspective." *Bull. Amer. Meteor. Soc.,* **66,** 795–801.

Heidinger, A. K., C. O'Dell, R. Bennartz, and T. Greenwald, 2006: The successive-order-of-interaction radiative transfer model. Part I: Model development. *J. Appl. Meteor. Climatol.,* **45,** 1388–1402.

Heymsfield, A. J., S. Matrosov, and B. Baum, 2003: Ice water path–optical depth relationships for cirrus and deep stratiform ice cloud layers. *J. Appl. Meteor.,* **42,** 1369–1390.

Hibbard, W. L., B. E. Paul, D. A. Santek, C. R. Dyer, A. L. Battaiola, and M. F. Voidrotmartinez, 1994: Interactive visualization of earth and space science computations. *Computer,* **27,** 65–72.

Hong, S., and J. J. Lim, 2006: The WRF single-moment 6-class microphysics scheme (WSM6). *J. Korean Meteor. Soc.,* **42,** 129–151.

Houze, R. A., Jr., 2004: Mesoscale convective systems. *Rev. Geophys.,* **42,** RG4003, doi:10.1029/2004RG000150.

Kain, J. S., S. R. Dembek, S. J. Weiss, J. L. Case, J. J. Levit, and R. A. Sobash, 2010: Extracting unique information from high-resolution forecast models: Monitoring selected fields and phenomena every time step. *Wea. Forecasting,* **25,** 1536–1542.

Lazzara, M. A., and Coauthors, 1999: The Man Computer Interactive Data Access System: 25 years of interactive processing. *Bull. Amer. Meteor. Soc.,* **80,** 271–284.

McMillin, L. M., L. J. Crone, M. D. Goldberg, and T. J. Kleespies, 1995: Atmospheric transmittance of an absorbing gas, 4: OPTRAN: A computationally fast and accurate transmittance model for absorbing gases with fixed and variable mixing ratios at variable viewing angles. *Appl. Opt.,* **34,** 6269–6274.

Mitchell, D. L., 2000: Parameterization of the Mie extinction and absorption coefficients for water clouds. *J. Atmos. Sci.,* **57,** 1311–1326.

Mostek, A., and Coauthors, 2004: VISIT: Bringing training to Weather Service forecasters using a new distance-learning tool. *Bull. Amer. Meteor. Soc.,* **85,** 823–829.

Otkin, J. A., and T. J. Greenwald, 2008: Comparison of WRF model-simulated and MODIS-derived cloud data. *Mon. Wea. Rev.,* **136,** 1957–1970.

——, ——, J. Sieglaff, and H.-L. Huang, 2009: Validation of a large-scale simulated brightness temperature dataset using SEVIRI satellite observations. *J. Appl. Meteor. Climatol.,* **48,** 1613–1626.

Raymond, W. H., and R. M. Aune, 2003: Conservations of moisture in a hybrid Kuo-type cumulus parameterization. *Mon. Wea. Rev.,* **131,** 771–779.

Reed, B., C. W. Siewert, R. S. Schneider, G. L. Hufford, B. Entwhistle, M. DeMaria, D. Reynolds, and M. J. Brennan, 2011: GOES-R Proving Ground—Demonstrating GOES-R products in 2010. Preprints, *27th Conf. on Interactive Information Processing Systems (IIPS),* Seattle, WA, Amer. Meteor. Soc., J10.1. [Available online at http://ams.confex.com/ams/91Annual/webprogram/Paper177076.html.]

Schiavone, J. A., and T. V. Papathomas, 1990: Visualizing meteorological data. *Bull. Amer. Meteor. Soc.,* **71,** 1012–1020.

Schmit, T. J., M. M. Gunshor, W. P. Menzel, J. Li, S. Bachmeier, and J. J. Gurka, 2005: Introducing the next-generation Advanced Baseline Imager on GOES-R. *Bull. Amer. Meteor. Soc.,* **86,** 1079–1096.

Seemann, S. W., E. E. Borbas, R. O. Knuteson, G. R. Stephenson, and H.-L. Huang, 2008: Development of a global infrared land surface emissivity database for application to clear-sky sounding retrievals from multispectral satellite radiance measurements. *J. Appl. Meteor. Climatol.,* **47,** 108–123.

Shuman, F. G., 1989: History of numerical weather prediction at the National Meteorological Center. *Wea. Forecasting,* **4,** 286–296.

Skamarock, W. C., J. B. Klemp, J. Dudhia, D. O. Gill, D. M. Barker, W. Wang and J. G. Powers, 2005: A description of the Advanced Research WRF version 2. NCAR Tech. Note NCAR/TN-468+STR, 88 pp.

Suchman, D., B. Auvine, and B. Hinton, 1981: Determining economic benefits of satellite data in short-range forecasting. *Bull. Amer. Meteor. Soc.,* **62,** 1458–1465.

Weisman, M. L., C. Davis, W. Wang, K. W. Manning, and J. B. Klemp, 2008: Experiences with 0–36-h explicit convective forecasts with the WRF-ARW model. *Wea. Forecasting,* **23,** 407–437.

Weldon, R. B., and S. J. Holmes, 1991: Water vapor imagery. NOAA Tech. Rep. NESDIS 57, 213 pp.